CHAPTER 3

RECONSTRUCTION WITH TWIN-IMAGE SUPPRESSION

3.1. Introduction

Digital reconstruction from in-line holograms is accomplished by simulating the corresponding physical process in Chapter 2. Having in mind the idea of extracting information related to object distribution from an in-line hologram, it is natural to ask how succesful the digital simulators are to this end. The results of Chapter 2 demonstrate that the digital reconstruction from optical holograms are already superior compared to the optical reconstructions. (See Figs.28-33) As indicated in the formulation of section 2.2, the major problem of the reconstructions is the existence of the contaminating twin-image. This can also be clearly seen from any one of the reconstruction pictures of chapter 2, where the desired object distribution is superposed on a strong background, which is the hologram of the same object at a distance twice of that of the recording (twin-image). Even though the optical reconstruction is worse than the digital one because of random noise and system imperfections, both of them suffer strongly from the twin-image effect. The twin-image effect is in the very nature of the reconstruction process (either optical or digital) of Chapter 2, because of two reasons: a) the inevitable "magnitude square" operation (only intensity can be recorded optically) of optical in-line hologram recording, and b) the reconstruction procedure used. However, since the decoding of optical holograms is to be performed digitally in our system, there is no reason to simply simulate the optical reconstruction, as done in Chapter 2. Instead, having the infinite flexibility of a computational procedure, it may be possible to formulate some new reconstruction (decoding) methods which perform better than the fixed conventional reconstruction

(either optical or digital) process. (From now on the reconstructions based on the formulation given in Chapter 2 will be called "conventional" reconstructions. Since both digital and the optical reconstructions are formulated in the same way, they are both conventional reconstructions. The digital ones are, in a sense, the best conventional reconstructions because of the reasons already mentioned.)

Such a reconstruction algorithm which suppresses the twin-image but preserves the linearity of the object distribution, is presented in this chapter, for the class of real object distributions. Complete mathematical structure of the proposed algorithm is given together with its physical interpretation. At the end of the chapter, pictorial results are compared with conventional reconstructions. Also, the "goodness" of the individual reconstructions are numerically obtained using a proper "performance measure", for both of the reconstructions.

Together with simple non-linear post processing techniques as given in Chapter 4, the holograms of certain type of input object distributions can be fully decoded, so that the resultant image is ready for further "image analysis".

3.2. The Approximate Inverse Filter

Lets start with the hologram as given by eq.(2.7). It is concluded in Chapter 2 that the cross-term is negligible for most of the cases. In addition to this, if the input object distribution $a(x,y)$ is a real function, then the second and third terms can be merged to get,

$$\begin{aligned} I_z(x,y) &= 1 - a(x,y) ** \left[h_Z^*(x,y) + h_z(x,y)\right] , \\ &= 1 - 2a(x,y) ** \mathrm{Re}\left\{h_z(x,y)\right\} . \end{aligned} \tag{3.1}$$

Therefore, the hologram $I_z(x,y)$ itself can be modelled as the (DC shifted) output of a linear system, whose impulse response is $g(x,y)$, where,

$$g(x,y) \equiv 2\,\mathrm{Re}\{h_z(x,y)\} \ . \tag{3.2}$$

Therefore, if the impulse response $g(x,y)$ had an inverse, $a(x,y)$ could be recovered by linear inverse filtering. Unfortunately, it does not have an inverse. This can be easily seen from the Fourier transform of the impulse response, i.e.,

$$\begin{aligned} G(u,v) = \mathcal{F}\left\{g(x,y)\right\} &= \mathcal{F}\left\{\frac{2}{\lambda z}\sin\frac{\pi}{\lambda z}(x^2+y^2)\right\} \ , \\ &= 2\cos\frac{\lambda z}{4\pi}(u^2+v^2) \ , \end{aligned} \tag{3.3}$$

where, u and v are the transform domain variables. The inverse would be $1/G(u,v)$, which is not defined because $G(u,v)$ has uncountably infinite number of zeros. Therefore, an inverse satisfying,

$$1 - G(u,v)^{-1}G(u,v) = 0 \qquad \forall (u,v) \in \mathbf{R}^2 \ . \tag{3.4}$$

cannot be found. Defining two new variables as,

$$q = \rho^2 = \frac{\lambda z}{4\pi}(u^2+v^2) \ , \tag{3.5}$$

we get $G(u,v) = G(q) = 2\cos q$. Now, lets seek an inverse $G^{-1}(q)$ which is defined everywhere, and satisfies,

$$\int_0^\infty \left| 1 - G^{-1}(q)G(q) \right| dq = 0 . \tag{3.6}$$

This requirement is equivalent to,

$$\int_0^\infty \left| 1 - G^{-1}(\rho)G(\rho) \right| \rho d\rho = 0 . \tag{3.7}$$

But this implies,

$$\int_0^{2\pi} \int_0^\infty \left| 1 - G^{-1}(\rho)G(\rho) \right| \rho d\rho \, d\Theta = 0 . \tag{3.8}$$

If Θ is chosen to be,

$$\cos\Theta = \frac{v}{(u^2+v^2)^{1/2}} , \tag{3.9}$$

then, the integral can be converted to cartesian coordinates to give,

$$\int_{-\infty}^{\infty} \int_{-\infty}^{\infty} \left| 1 - G^{-1}(u,v)G(u,v) \right| du \, dv = 0 . \tag{3.10}$$

Therefore, the inverse that we are looking for will be convergent in the sense of eq.(3.10).

Lets expand $\frac{1}{2\cos q}$ into its Fourier series. The expansion exists if the integrals,

$$a_k = \frac{1}{\pi}\int_{-\pi}^{\pi} \frac{1}{2\cos\tau}\cos k\tau\, d\tau \ ,$$
$$b_k = \frac{1}{\pi}\int_{-\pi}^{\pi} \frac{1}{2\cos\tau}\sin k\tau\, d\tau \ , \qquad (3.11)$$

exist. The integrals above can be evaluated to yield (see Ref.56 p.16 for.18),

$$a_k = \begin{cases} 1 & k=1,5,9\ldots \\ 0 & k=0,2,4\ldots \\ -1 & k=3,7,11\ldots \end{cases} \ , \qquad (3.12)$$

and from even symmetry of $\frac{1}{2\cos q}$,

$$b_k = 0 \ , \quad \forall k \ . \qquad (3.13)$$

Therefore, the formal Fourier series expansion of $\frac{1}{2\cos q}$ exists, and given by,

$$F\ .S.\ E.\left\{\frac{1}{2\cos q}\right\} = \sum_{k=0}^{\infty}(-1)^k\cos\left[(2k+1)\,q\right] \ . \qquad (3.14)$$

The existence of Fourier series expansion does not guarantee convergence in any sense in general [43]. If the function whose Fourier series expansion exists also has a finite $\mathbf{L}^2_{2\pi}$ norm, i.e., if,

$$\int_{-\pi}^{\pi} |f(x)|^2 \, dx < \infty , \tag{3.15}$$

then the Fourier series converges in mean square sense, if it exists. But,

$$\int_{-\pi}^{\pi} \left| \frac{1}{2\cos x} \right|^2 dx = \int_{0}^{\pi/2} \frac{1}{\cos^2 x} \, dx = \tan x \Big|_0^{\pi/2} = \infty . \tag{3.16}$$

Therefore, $\frac{1}{2\cos q} \notin \mathbf{L}^2_{2\pi}$, and the convergence of series is not guaranteed although it exists. Furthermore,

$$\int_{-\pi}^{\pi} \left| \frac{1}{2\cos x} \right| dx = 2 \int_{0}^{\pi/2} \frac{1}{\cos x} \, dx = 2 \, Ln \left| \frac{1}{\cos x} + \tan x \right| \Big|_0^{\pi/2} = \infty . \tag{3.17}$$

Thus, the convergence of the series in any $\mathbf{L}^p_{2\pi}$ norm, $1 \le p < \infty$, is not guaranteed.

Lets check if a windowed Fourier series expansion of $\frac{1}{2\cos q}$ satisfies the convergence requirement given in eq.(3.6). Suppose that a window function is specified as,

$$W(k) = \begin{cases} 1 & k=0 \\ \left\{\dfrac{M-1-[\![\log_2 k]\!]}{M}\right\} & 1 \le k \le 2^{M-1}-1 \\ 0 & else \end{cases} \quad . \tag{3.18}$$

The reason why the window function is selected like this will be clear in the next section: it has a very descriptive physical interpretation. Thus the series expansion weighted by the window function,

$$\sum_{k=0}^{2^{M-1}-1} W(k)(-1)^k \cos(2k+1)q \quad , \tag{3.19}$$

becomes,

$$\cos q + \sum_{k=1}^{2^{M-1}-1} \left\{\frac{M-1-[\![\log_2 k]\!]}{M}\right\}(-1)^k \cos(2k+1)q \equiv G_M^{-1}(q) \tag{3.20}$$

To prove that the series expansion, $G_M^{-1}(q)$, given above satisfies the convergence criteria of eq.(3.6) in the limit $M \to \infty$, lets start with

$$G_M^{-1}(q)G(q) = G_M^{-1}(q)\,2\cos q =$$

$$= 2\cos^2 q + 2\sum_{k=1}^{2^{M-1}-1}\left\{\frac{M-1-[\![\log_2 k]\!]}{M}\right\}(-1)^k \cos q\,\cos(2k+1)q \ .$$

$$= 1 + \cos 2q + \sum_{k=1}^{2^{M-1}-1}\left\{\frac{M-1-[\![\log_2 k]\!]}{M}\right\}(-1)^k\left\{\cos(2kq) + \cos(2k+2)q\right\}, \quad (3.21)$$

$$= 1 + \cos 2q + \sum_{k=1}^{2^{M-1}-1}\left\{\frac{M-1-[\![\log_2 k]\!]}{M}\right\}(-1)^k \cos(2kq) +$$

$$\sum_{k=1}^{2^{M-1}-1}\left\{\frac{M-1-[\![\log_2 k]\!]}{M}\right\}(-1)^k \cos 2(k+1)q \ .$$

The equation above can be rewritten as,

$$G_M^{-1}(q)G(q) = 1 + \cos 2q - \frac{M-1}{M}\cos 2q - \frac{1}{M}\cos 2^M q$$

$$+ \sum_{k=2}^{2^{M-1}-1}\frac{-[\![\log_2 k]\!] + [\![\log_2(k-1)]\!]}{M}(-1)^k \cos(2kq) \ . \quad (3.22)$$

The term in the summation above can be reduced to,

$$\frac{-[\![\log_2 k]\!] + [\![\log_2(k-1)]\!]}{M}(-1)^k \cos(2kq) = \begin{cases} 0 & k \neq 2^r \\ \dfrac{-1}{M}\cos 2^{r+1}q & k = 2^r \end{cases} \quad (3.23)$$

where, r is a positive integer. Thus the term with the summation in eq.(3.22) becomes,

$$\frac{-1}{M} \sum_{m=2}^{M-1} \cos 2^m q \tag{3.24}$$

Therefore, eq.(3.22) can be written as,

$$G_M^{-1}(q)G(q) = 1 + \frac{1}{M}\cos 2q - \frac{1}{M}\sum_{m=2}^{M}\cos 2^m q \ . \tag{3.25}$$

The behaviour of the third term above is particularly important as $M \to \infty$. Using theory of "distribution of sequences modulo 1" (see Appendix E and Ref.47), it can be shown that,

$$\lim_{M\to\infty} \frac{1}{M} \sum_{m=2}^{M} \cos 2^m q = \begin{cases} 0 & \frac{q}{\pi} \ irrational, \\ K(q) & \frac{q}{\pi} \ rational, \end{cases} \tag{3.26}$$

where $|K(q)| \leq 1$. Therefore,

$$G_M^{-1}(q)G(q) = \begin{cases} 1 & \frac{q}{\pi} \ irrational, \\ 1-K(q) & \frac{q}{\pi} \ rational. \end{cases} \tag{3.27}$$

Now, it must be shown that,[1]

[1] The integral is a Lebesgue integral. (Because of the nature of the integrand, Riemmann integral is meaningless.)

$$\int_{-\pi}^{\pi} \left| 1 - 2\cos q \; G_{\infty}^{-1}(q) \right| dq \; = \; 0. \tag{3.28}$$

Defining P_{ir} as the ratio of all irrational numbers to all numbers in the interval $[-\pi , \pi]$, and from eq.(3.27),

$$\int_{-\pi}^{\pi} \left| 1 - 2\cos q \; G_{\infty}^{-1}(q) \right| dq \; \leq \; 0 \; P_{ir} \; + \; Q(1-P_{ir}) \; = \; Q\,(1-P_{ir}) \; , \tag{3.29}$$

where, Q is the upper bound of $\left| 1 - G_{\infty}^{-1}(q) G(q) \right|$, which is already shown in eq.(3.27) to be finite. Since the irrational numbers form a set with measure 2π on the interval $[-\pi,\pi]$, $P_{ir} = 1$. Then the result above becomes,

$$\int_{-\pi}^{\pi} \left| 1 - 2\cos q \; G_{\infty}^{-1}(q) \right| dq \; = \; 0 \; . \tag{3.30}$$

□

Therefore, the filter function,

$$G_M^{-1}(u,v) \; = \; \cos\frac{\lambda z}{4\pi}(u^2+v^2) \; + \; \sum_{k=1}^{2^{M-1}-1} \left\{ \frac{M-1-[\![log_2 k]\!]}{M} \right\} S_k(u,v) \; , \tag{3.31}$$

$$S_k(u,v) \; = \; (-1)^k \cos\frac{\lambda z}{4\pi}(2k+1)(u^2+v^2) \; .$$

is a series approximation to the Fourier transform of inverse filter, and converges to it in

the sense of eq.(3.10) as $M \to \infty$. Note that the proof can be easily extended for convergence of the form,

$$\int_{-\pi}^{\pi} \left| 1 - G_{\infty}^{-1}(q) G(q) \right|^{p} dq \quad , \tag{3.32}$$

for $0 < p < \infty$, simply by having Q of eq.(3.29) as the upper bound of $\left| 1 - G_{\infty}^{-1}(q) G(q) \right|^{p}$, which is bounded.

Therefore, if the hologram, $I_z(x,y)$, is filtered by the filter $g_M^{-1}(x,y)$ where,

$$g_M^{-1}(x,y) = \mathcal{F}^{-1}\left\{ G_M^{-1}(u,v) \right\} , \tag{3.33}$$

then the result will have the original object distribution $a(x,y)$ and an undesired residual term.

Now lets go back to the conventional reconstruction process, and derive it for the case of negligible non-linear cross-terms:

$$\varphi_z(x,y) = 1 + I_z(x,y) ** h_z(x,y) \ . \tag{3.34}$$

Then the intensity of conventional reconstruction is given by,

$$R_z(x,y) = 1 + 2\,\mathrm{Re}\left\{ I_z(x,y) ** h_z(x,y) \right\} + cross\text{-}terms \ . \tag{3.35}$$

Since the hologram $I_z(x,y)$ is always real, the reconstruction above becomes (cross-terms are neglected),

$$\begin{aligned} R_z(x,y) &= 1 + 2I_z(x,y) ** \mathrm{Re}\left\{h_z(x,y)\right\} , \\ &= 1 + I_z(x,y) ** g(x,y) , \end{aligned} \tag{3.36}$$

where, $g(x,y)$ is defined by eq.(3.2). Therefore, conventional reconstruction process can also be approximated by a linear operation (convolution), like recording, even though there is a non-linear magnitude square operation. The non-linear terms are negligible due to strong DC bias. Note that the convolution kernel $g(x,y)$ is equal (within a gain factor) to the first term of the series expansion of the approximate inverse filter $G_M^{-1}(u,v)$. (See eq.(3.3).). In other words,

$$2G_1^{-1}(u,v) = G(u,v) . \tag{3.37}$$

Therefore, conventional reconstruction is equivalent to using approximate inverse filter with only first term, whether $a(x,y)$ is real or complex.

3.3. Physical Interpretation of the Approximate Inverse Filter

A linear filter which approximates the exact inverse filter is presented in the previous section. The approximation is a truncated series expansion in the frequency domain, (u,v). The basis functions for the expansion are of the form $\cos\frac{\lambda z}{4\pi}(2k+1)(u^2+v^2)$, where k is an integer. The approximation has a nice physical interpretation. In fact, the idea for the

form of the filter is obtained from this physical procedure in the first place.

Lets start with the reconstruction field as given in eq.(2.12). Instead of taking the intensity of this field, lets have the real and imaginary parts, and define $b_z(x,y)$ and $q_z(x,y)$ as:

$$\begin{aligned} \mathrm{Re}\{\varphi_z(x,y)\} &= 2 - a(x,y) - a(x,y) ** \mathrm{Re}\{h_{2z}(x,y)\} \\ &\equiv 2 + b_z(x,y), \end{aligned} \tag{3.38.a}$$

and,

$$\begin{aligned} \mathrm{Im}\{\varphi_z(x,y)\} &= -a(x,y) ** \mathrm{Im}\{h_{2z}(x,y)\}. \\ &\equiv q_z(x,y). \end{aligned} \tag{3.38.b}$$

As observed from the equations above, the desired component of the reconstruction is only in $b_z(x,y)$. In addition to that, $b_z(x,y)$ has the real part of the undesired twin-image term. On the other hand, $q_z(x,y)$ has only the imaginary part of the twin-image component. This is the consequence of having pure real input object distribution function. Therefore, taking the intensity makes the twin-image effect worse, because of the additional effect due to the imaginary part, compared to taking the real part of the field. An important observation is that $q_z(x,y)$ is itself very similar to a hologram, at distance $2z$: $\mathrm{Im}\{h_{2z}(x,y)\}$ is the convolution kernel, instead of $\mathrm{Re}\{h_{2z}(x,y)\}$ (see eq.(3.1) and note that the DC part is not important since the overall algorithm is going to be linear). So, $q_z(x,y)$ can be used as a new hologram to reconstruct the object again. In fact, using the properties:

$$\begin{aligned} \mathrm{Im}\{h_{nz}(x,y)\} ** \mathrm{Im}\{h_{nz}(x,y)\} &= \tfrac{1}{2}\delta(x,y) - \tfrac{1}{2}\mathrm{Re}\{h_{2nz}(x,y)\}, \\ \mathrm{Im}\{h_{nz}(x,y)\} ** \mathrm{Re}\{h_{nz}(x,y)\} &= \tfrac{1}{2}\mathrm{Im}\{h_{2nz}(x,y)\} \end{aligned} \tag{3.39}$$

it can be shown that,

$$\begin{aligned} q_z(x,y) ** 2Im\{h_{2z}(x,y)\} &= -2a(x,y) ** \mathrm{Im}\{h_{2z}(x,y)\} ** \mathrm{Im}\{h_{2z}(x,y)\} \\ &= -a(x,y) ** \delta(x,y) + a(x,y) ** \mathrm{Re}\{h_{4z}(x,y)\}, \\ &= -a(x,y) + a(x,y) ** \mathrm{Re}\{h_{4z}(x,y)\}, \\ &= p_{2z}(x,y), \end{aligned} \tag{3.40.a}$$

and,

$$\begin{aligned} q_z(x,y) ** 2Re\{h_{2z}(x,y)\} &= -2a(x,y) ** \mathrm{Im}\{h_{2z}(x,y)\} ** \mathrm{Re}\{h_{2z}(x,y)\} \\ &= -a(x,y) ** \mathrm{Im}\{h_{4z}(x,y)\}. \\ &= q_{2z}(x,y). \end{aligned} \tag{3.40.b}$$

Eq.(3.40) can be generalized to have,

$$p_{2^n z}(x,y) = q_{2^{n-1}z}(x,y) ** 2Im\{h_{2^n z}(x,y)\}, \tag{3.41.a}$$

$$q_{2^n z}(x,y) = q_{2^{n-1}z}(x,y) ** 2Re\{h_{2^n z}(x,y)\}. \tag{3.41.b}$$

The important implication of eq.(3.41) is that at every recursion of it, a new reconstruction,

$p_{2^n z}(x,y)$, which has the desired component $-a(x,y)$ in it, is made. All of these reconstructions have the twin-image effect $a(x,y) ** \mathrm{Re}\{h_{2^{n+1}z}(x,y)\}$, corrupting the desired component. But the twin-images at every stage, n, are different from each other: they are the holograms of $a(x,y)$ at a distance $2^{n+1}z$. Suppose that the average of all reconstructions, that is, all $p_{2^n z}(x,y)$'s and $b_z(x,y)$, is taken. Since all of these terms has the desired component $a(x,y)$ in them, the average also has it unchanged. However, since the twin-image terms are different, they don't add up constructively, thus they tend to cancel each other. So, the final result is given by,

$$\begin{aligned} d_M(x,y) &= \frac{1}{M}\left\{ b_z(x,y) + \sum_{n=1}^{M-1} p_{2^n z}(x,y) \right\} \\ &= -a(x,y) + a(x,y) ** \frac{1}{M}\left[-Re\{h_{2z}(x,y)\} + \sum_{n=1}^{M-1} \mathrm{Re}\{h_{2^{n+1}z}(x,y)\} \right]. \end{aligned} \tag{3.42}$$

Equation above can be written as the output of a convolution as,

$$d_M(x,y) = -a(x,y) ** \left[\delta(x,y) + \frac{1}{M}\mathrm{Re}\{h_{2z}(x,y)\} - \frac{1}{M}\sum_{n=2}^{M} \mathrm{Re}\{h_{2^n z}(x,y)\} \right]. \tag{3.43}$$

The Fourier transform of the convolution kernel above is,

$$1 + \frac{1}{M}\cos\frac{2\lambda z}{4\pi}(u^2+v^2) - \frac{1}{M}\sum_{n=2}^{M} \cos\frac{2^n \lambda z}{4\pi}(u^2+v^2) \tag{3.44}$$

which is exactly the righthand side of eq.(3.25), with the change of variables as in eq.(3.5).

The convergence properties of the kernel,

$$\left| \delta(x,y) + \frac{1}{M} \mathrm{Re}\{h_{2z}(x,y)\} - \frac{1}{M} \sum_{n=2}^{M} \mathrm{Re}\{h_{2^n z}(x,y)\} \right|, \tag{3.45}$$

is even better than the convergence of its Fourier transform. In the previous section it is shown that the Fourier transform of the kernel above converges in $\mathbf{L}^p_{2\pi}$ norm to 1. To see the convergence of the kernel itself, lets start with,

$$\frac{1}{M} \sum_{n=2}^{M} \mathrm{Re}\left\{h_{2^n z}(x,y)\right\} = \frac{1}{M} \sum_{n=2}^{M} \frac{1}{\lambda 2^n z} \sin \frac{\pi}{\lambda 2^n z}(x^2+y^2) \ . \tag{3.46}$$

But, the absolute value of the expression above is less than,

$$\frac{1}{M} \frac{1}{\lambda z} \sum_{n=2}^{M} \frac{1}{2^n} \ . \tag{3.47}$$

The expression above is a power series, so it can be evaluted as,

$$\frac{1}{\lambda z} \frac{1}{M} \left[\frac{1}{2} - \left(\frac{1}{2}\right)^M \right], \tag{3..48}$$

which goes to 0 as $M \to \infty$. Convergence of the upper bound is monotone. Since the upper

bound goes to 0, the expression itself goes to zero, too. The second term $\frac{1}{M}\mathrm{Re}\{h_{2z}(x,y)\}$ also goes to 0, therefore, the kernel converges to $\delta(x,y)$ as $M \to \infty$. The convergence is *pointwise*. Note that the upper bound given above is a loose one. Therefore, it is expected that the expression itself goes to zero much faster than the upper bound.

If a convolution kernel goes to zero in the limit, it does not necessarily imply that the result of convolution also goes to zero. However, this is guaranteed if the input function to the convolution has finite energy, and a finite Fourier transform. Thus, if the input function $a(x,y)$ has these properties, the eq.(3.43) reduces to,

$$d_{\infty}(x,y) = -a(x,y) \ , \tag{3.49}$$

which is the desired reconstruction. The discussion above is another proof that the approximate filter given by eq.(3.31) converges to the exact inverse filter.

Analogy: The overall algorithm explained above is analogous to having the cross-sectional samples from a volume hologram at distances $2^k z$, for k=0,1,2,... . Then these samples are reconstructed. As the number of samples increases, the resultant effect is like the physical volume hologram: no twin image exists in the reconstruction. Note that none of the samples are recorded physically, but obtained from a single hologram by computation.

The algorithm is summarized in Fig.37.

3.4. Digital Implementation of the Algorithm

The algorithm given in previous sections can be implemented completely in Fourier transform domain. Thus, the convolutions shown in Fig.37. are converted to

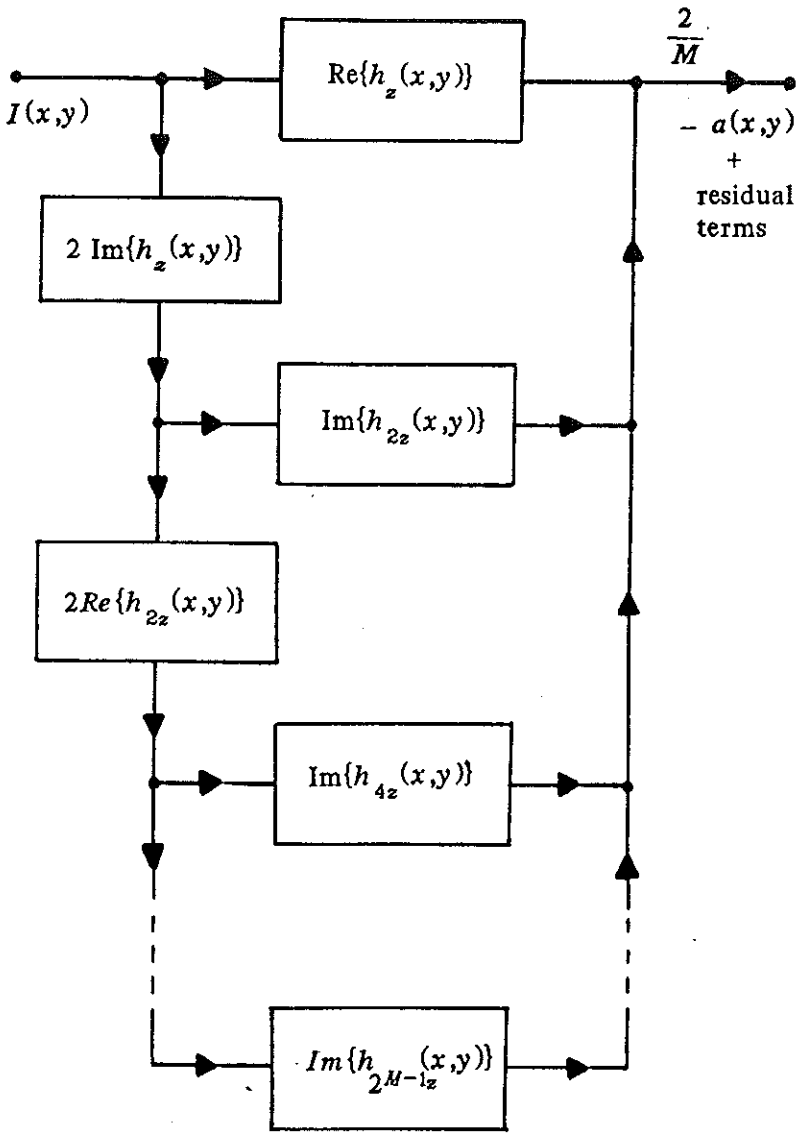

Figure 37. Reconstruction with twin-image suppression.

multiplications. Since the Fourier transforms of all convolution kernels of Fig.37. are known analytically as,

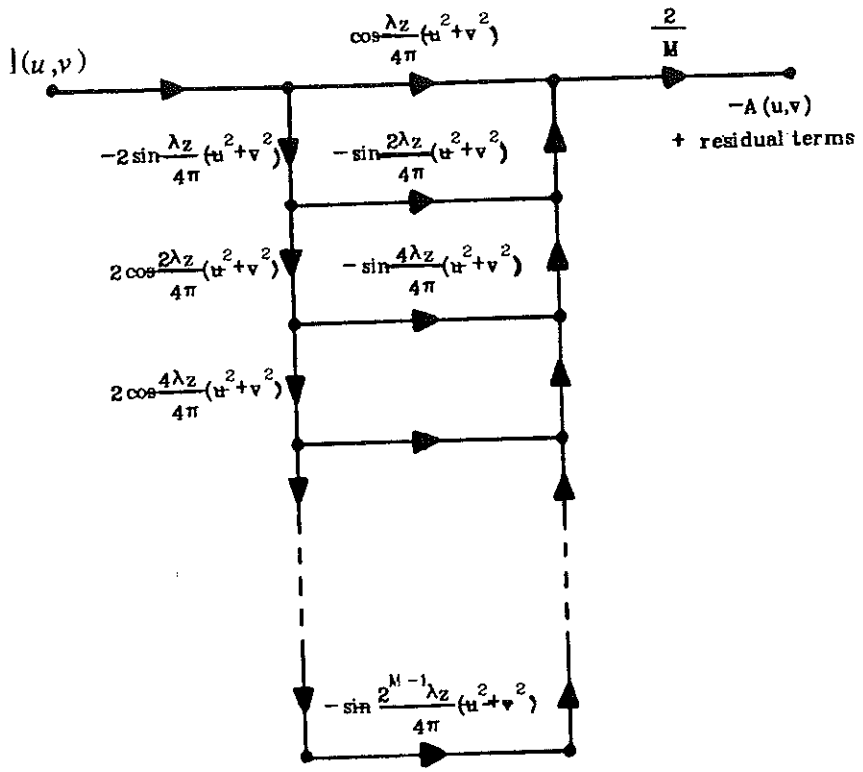

Figure 38. The twin-image suppression algorithm in Fourier transform domain.

$$\mathcal{F}\left\{\mathrm{Re}\{h_{kz}(x,y)\}\right\} = \cos\frac{\lambda kz}{4\pi}(u^2+v^2)\ ,$$
$$\mathcal{F}\left\{\mathrm{Im}\{h_{kz}(x,y)\}\right\} = -\sin\frac{\lambda kz}{4\pi}(u^2+v^2)\ , \tag{3.50}$$

the system can be redrawn in the transform domain as in Fig.38. The filter function could be computed directly by using the series form as given by eq.(3.31). However, the form suggested by Fig.38 is exactly equivalent and much more efficient. The equivalence can be

easily seen if the Fig.38 is converted to the form given in Fig.39, simply by using trigonometric formulas. Then each branch becomes a partial sum of the Fourier series expansion (with the change of variables as in eq.(3.5)) of $\frac{1}{2\cos q}$. Eq.(3.31) can be obtained by summing the same terms of each branch separately. It is interesting to observe that each branch is a partial sum of the Fourier series expansion given above. To perform the computation digitally, the continuous functions of Fig.38 are digitized, and circular convolutions are performed as in Chapter 2 section 3. The algorithm in discrete domain is shown in Fig.40. The effect of sampling in Fourier transform domain is analyzed in detail in that section. Note that, at every stage, the spatial extent of the twin-image doubles. This will show itself as increased overlappings in circular convolutions: the twin-image

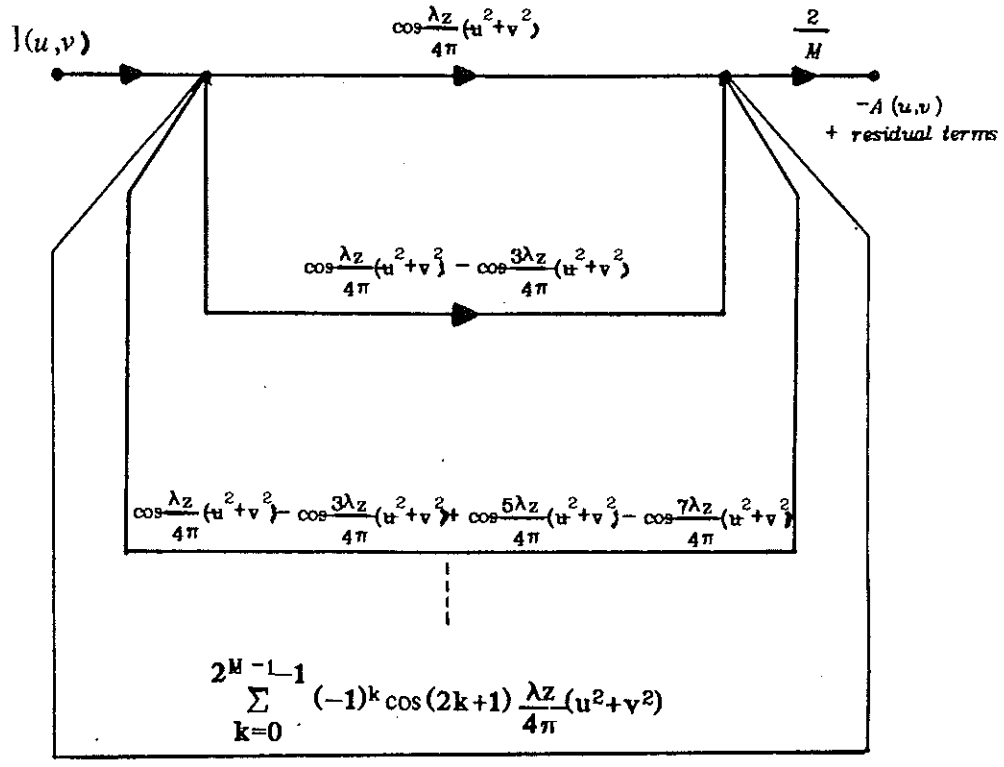

Figure 39. Equivalent form of the filter of Fig.38.

even from periods quite far away will add up. To decrease the effect of this, the convolution size must be chosen as large as possible.

3.4.1. The Results

The discrete algorithm shown in Fig.40 is implemented at SUNY Buffalo LAPES Laboratory image processing system. The Fortran subroutine is given in Appendix C. The initial hologram size in the following pictures is 256×256 and has 8 bit (256 level) gray levels. The data is zero extended to size 512×512 (the input size is doubled in each direction), to reduce the overlapping. Then 512×512 discrete Fourier transform of this

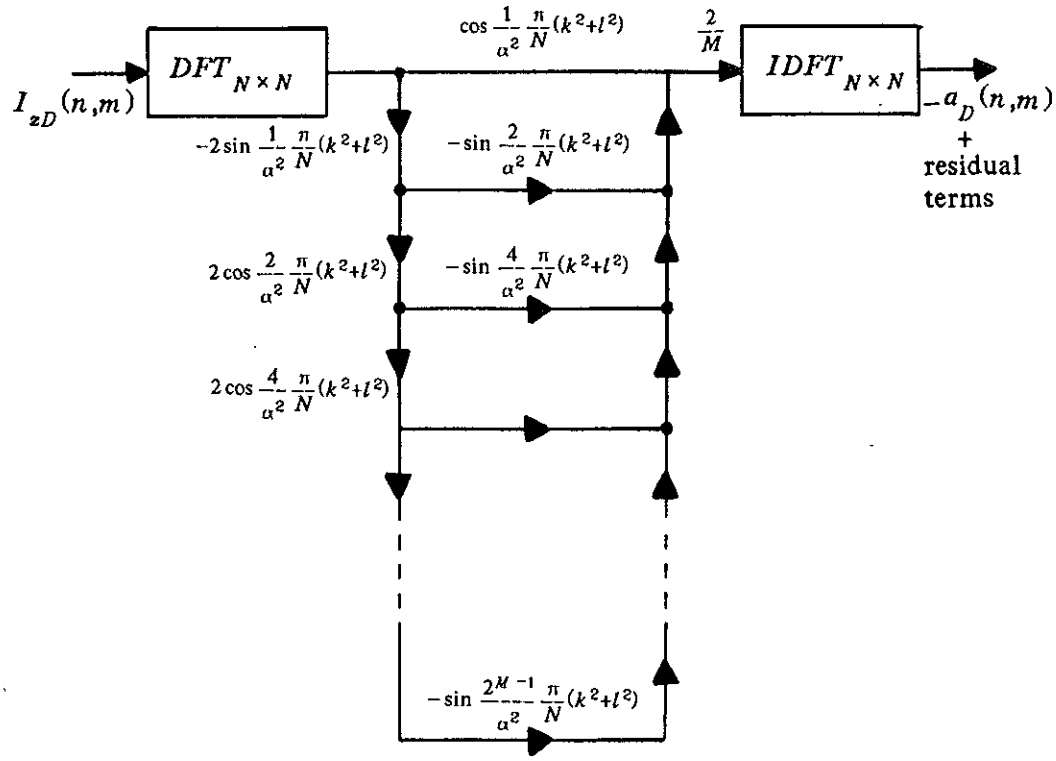

Figure 40. The discrete version of the system shown in Fig.38 (size is assumed square, N × N).

hologram is taken using a fast Fourier transform algorithm. The procedure of Fig.40 is then implemented with $N = 512$. 512×512 inverse discrete Fourier transform is used for the final step, and then the only that 256×256 portion of the result corresponding the original input is displayed. Note that neither the absolute gain nor the DC shift is important for the digital implementation, since the output is normalized to utilize the 8-bit dynamic range to the full extent.

Some applications of the twin-image suppression using the linear filter designed in this chapter is shown by the following pictures.

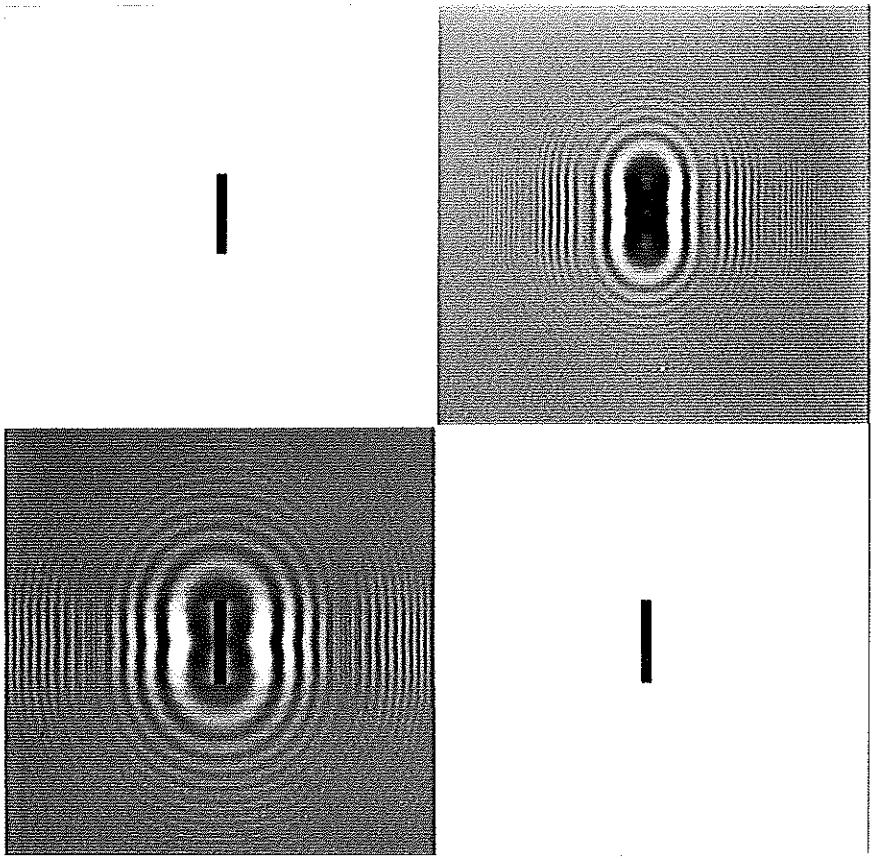

Figure 41. Comparison of conventional reconstruction and reconstruction with twin-image suppression.

a) A synthesized object.
b) Hologram of a synthesized object. $\alpha = 1$.
c) Conventional reconstruction (Type I).
d) Reconstruction with twin-image suppression. M=5.

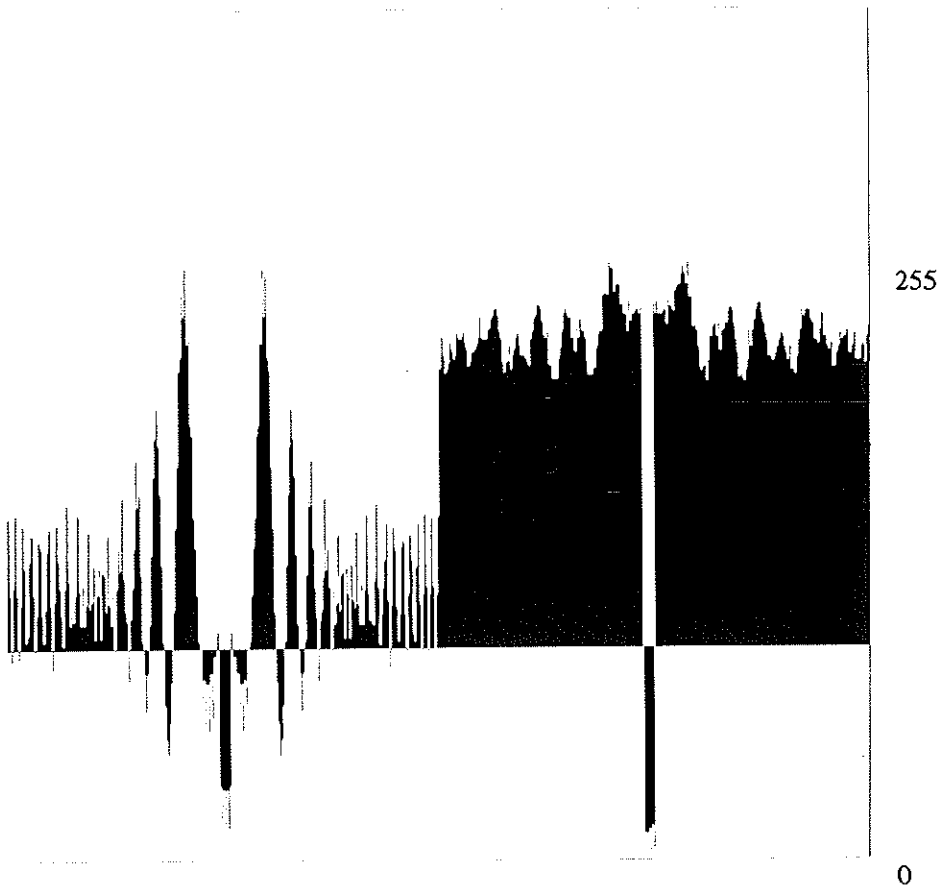

Figure 42. The profiles of the two reconstructions of Fig.41. through the center.

a) Conventional reconstruction.
b) Reconstruction with twin-image suppression.

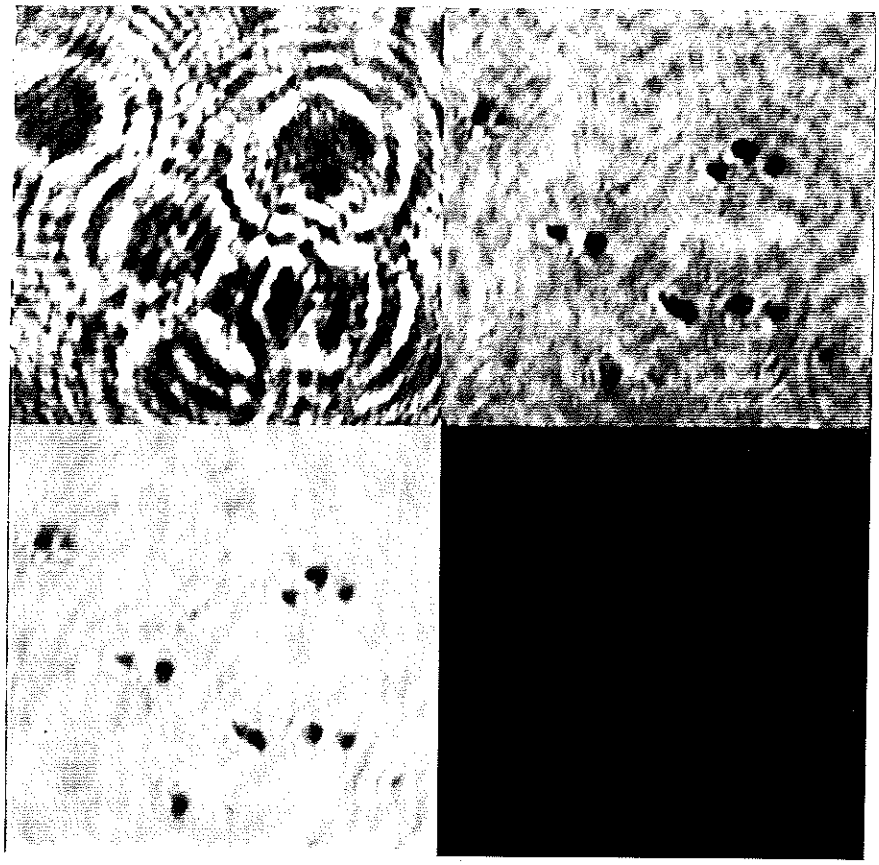

Figure 43. Comparison of conventional reconstruction and reconstruction with twin-image suppression.

a) A digitized optical hologram portion. $\alpha = 0.541$.
b) Conventional reconstruction (Type I).
c) Reconstruction with twin-image suppression. M=3.

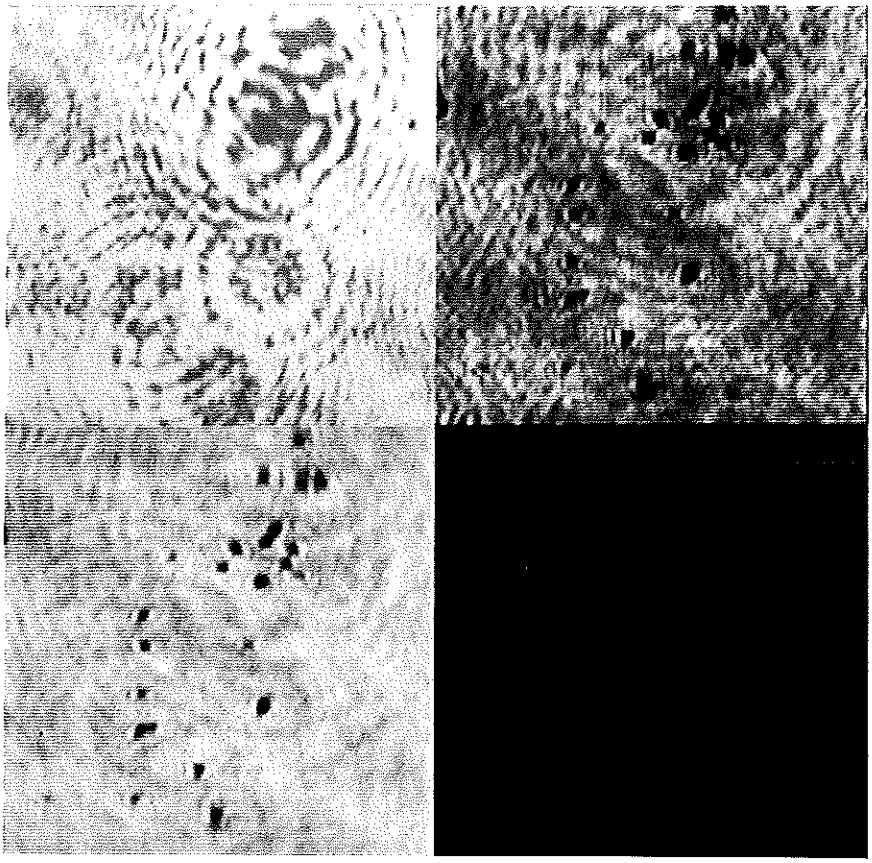

Figure 44. Comparison of conventional reconstruction and reconstruction with twin-image suppression.

a) A digitized optical hologram portion. $\alpha = 0.650$.
b) Conventional reconstruction (Type I).
c) Reconstruction with twin-image suppression. M=2.

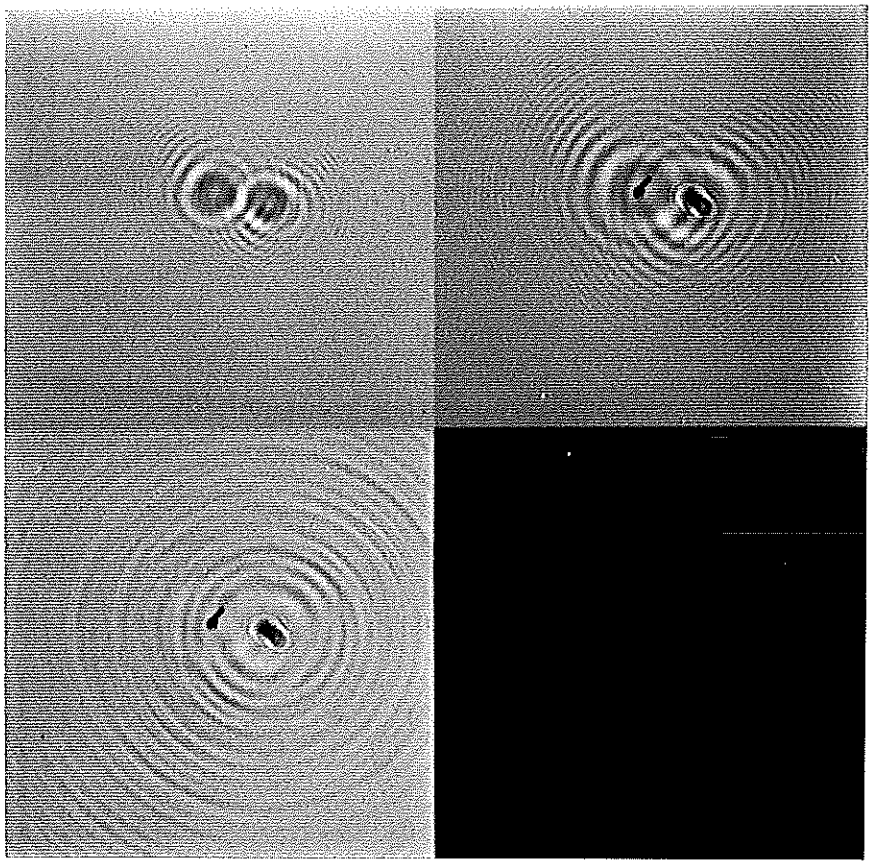

Figure 45. Comparison of conventional reconstruction and reconstruction with twin-image suppression for a double exposed hologram.

a) A simulated double exposure hologram.
b) Conventional reconstruction (Type I). $\alpha = 1.15$.
c) Reconstruction with twin-image suppression. M=4.

The approximate inverse filter succesfully suppresses the twin-image corresponding to the in-focus reconstruction. However, the two other components corresponding to the out-of-focus object can not be suppressed by the filter. (See Chapter 2 section 5.)

The reduction in the background twin-image is numerically measured by computing the RMS deviation of the background, from the original DC level, for the results of Fig.41. The results are shown in Table 1.

TABLE 1 RMS errors of reconstructions (units of gray level)

	Conventional reconstruction	Reconstruction with twin-image suppression
Figure 41	30.90	6.25
Figure 43	42.02	17.77
Figure 44	38.68	15.90

As mentioned before, the individual pictures (four of them) of Fig.41. are displayed by normalizing their DC levels and the gains to achieve maximum dynamic gray-level range usage. This is taken into account and compansation is made for the accuracy of the RMS deviation measurements: To get the RMS deviation of an individual reconstruction from the original object, the DC level and the gain of that reconstruction (or equivalently the original object) is adjusted to have minimum deviation. The resultant error is again normalized to a constant gain (gain of the original input), so that comparisons are meaningful.

The same kind of measurements are also performed for the digital reconstruction of the optical holograms of Figs.43 and 44 . But, in this case, an area of the reconstructions where there are no objects is chosen, since the original values of objects are unknown. The assumption is that the background must be constant. Thus, the RMS deviation of the background portion is measured from a DC level which minimizes it. The measurements for the two reconstructions are made for the same region.

Another measure for the "goodness" of the reconstructions could be the "peak deviation". The results for this measure is given in Table 2.

TABLE 2 Peak-to-peak errors of reconstructions (units of gray level)

	Conventional reconstruction	Reconstruction with twin-image suppression
Figure 41	470	65
Figure 43	260	102
Figure 44	237	98

3.5. Comments

The approximate inverse filter and its convergence properties in space and transform domains are given for the continuous case. The filter is implemented in discrete domain. Therefore, the convergence properties are not valid for the discrete case. In fact, since every discretization incorporates sampling at *rationals*, then the discrete algorithm does not converge in the sense given in section 2, and 3. If desired, convergence can be guaranteed by choosing another window, instead of the one given by eq.(3.18). For example, the window function,

$$W_M(k) = \frac{\sin k\frac{\pi}{M}}{k\frac{\pi}{M}} \tag{3.51}$$

guarantees pointwise convergence (see Ref.44 p.65,71). It must be stressed here that what is expected from an approximate linear inverse filter is a reasonable reduction in the residual background, which is the twin-image in holography. An approximate inverse filter must

never be allowed to get too close to the exact inverse. Otherwise, it will possess many undesirable properties of the exact inverse, such as unreasonable gains close to the zeros of the filter whose inverse is approximated. Therefore, the filter given in this chapter is intended to be used with rather smaller number of terms (small M). As seen from the results presented in this chapter, it is satisfactory to have $M = 2–7$. At this order, the approximate filter is still quite far from the exact inverse, but it is a better approximation than having $M = 1$, which is the conventional reconstruction. So, it does not have the undesirable features of an exact inverse, and still increases the quality of the reconstructions. Since a close approximation is not required as mentioned above, a filter with better convergence properties is not necessarily a better choice.

It is definitely possible to use the generalized approach of deconvolution for the reconstruction. However, effective deconvolution algorithms, such as those based on probabilistic models and estimation, are computationally very long, and therefore practically restrictive because of the size of the problem. Other algorithms such as "constrained deconvolution" may be coupled to the presented approach provided that sufficient restrictions related to a specific in-line hologram application are well established. The approach given in this chapter makes no *a priori* assumptions about the input object distribution, except its realness. Therefore, it is a rather general technique, and could be used in many diverse hologram applications. Some other sophisticated deconvolution techniques such as "projections onto convex sets" also suffer from high computational requirements due to the size of the problem, and require additional *a priori* information (constraints) which are not well established for holography. As shown in Chapter 4, the results obtained by the approximate filter are sufficient for further, possibly non-linear, processing. It should also be noted here that it is the nice property given in eq.(2.10.a) of the convolution kernel, that makes the reconstruction much easier. Therefore, this property must be fully utilized to reduce the effort of decoding, before any attempt for

computationally long generalized approaches.

Another property of the approximate inverse filter of this chapter is that it is an edge-preserving filter. Even the lowest order terms distribute energy over all frequency ranges. Thus, approximate filtering of any order, does not result in low-pass smearing of edges of objects in $a(x,y)$. This property is fundamental for many applications where the objects consist of separate bodies (particles). For instance, analysis of particle shapes (all of the pictures related to optical holograms has particles as the object, in this dissertation) requires well preserved sharp edges. The reconstructions done by approximate inverse filtering are further processed by simple non-linear techniques for edge detection in Chapter 4.